2024 IEEE/RSJ International Conference on Intelligent Robots and Systems (IROS)
October 14-18, 2024. Abu Dhabi, UAE

6D Variable Virtual Fixtures for Telemanipulated Insertion Tasks

Stephan Andreas Schwarz[1] and Ulrike Thomas[1]

***Abstract*— Telemanipulation enables humans to perform tasks in dangerous environments without exposing them to any risk. The COVID-19 pandemic sadly showed, that these environments can also include the treatment and interaction with infected patients. Since human-robot interactions demand for low interaction forces yet high precision, telemanipulation often results in a high mental workload for the operator. To overcome this, we present a virtual guidance approach to perform telemanipulated insertion tasks. A nasopharyngeal swap sampling procedure is taken as use case. We extend our previously presented approach by adding an additional position fixture, introducing distance-dependent variable stiffness values and guaranteeing stability using energy tanks. Based on RGB-D data, the operator is guided towards a desirable insertion line while approaching the nostril. The distance-dependent stiffness values increase the smoothness of the fixture. Since variable stiffness values can result in unstable behavior, energy tanks for the fixtures are introduced. Experiments show the improvements compared to our previous approach. Further, a comparison between guided and unguided samplings performed by an expert user gives a first impression of the improvements resulting from the fixture.**

I. INTRODUCTION

The COVID-19 pandemic showed the dangers of infections that are transmitted over the air. While isolation is a good way to avoid an infection, direct contacts are currently unavoidable for some groups of people. Especially medical staff has to impose themselves to the patients to examine and treat them. In these cases, measures to reduce the probability of an infection exists, but are limited and it would be ideal to avoid direct contacts completely.

The concept of telemanipulation can be applied to achieve such a scenario. The operator can perform treatments from a remote environment by interacting with an input device. This interaction will be transmitted to the follower robot which performs the task. With this, individual treatment is possible while also maintaining the isolation of the patient. This concept is increasingly used in specialized applications like telemedicine but only rarely in more flexible applications. One reason is the safety aspect of these human-robot interactions. The interaction forces have to be small while in contact with patients. On the other side, high precision is required to perform, e.g., sampling tasks. Virtual fixtures that drag the operator to a desirable pose or away from a forbidden region are a suitable tool to improve these requirements.

In this work, we present a shared control approach that increases task performance while reducing the interaction forces of telemanipulated insertion tasks. Due to its recent presence, nasopharyngeal swab samplings are chosen as a suitable use case. A 6D vision-based virtual fixture is applied to guide the operator while approaching the nostril of the subject. Besides maintaining a desirable pose during swab insertion, the fixture also avoids unintentional deep and dangerous penetration of the nostril.

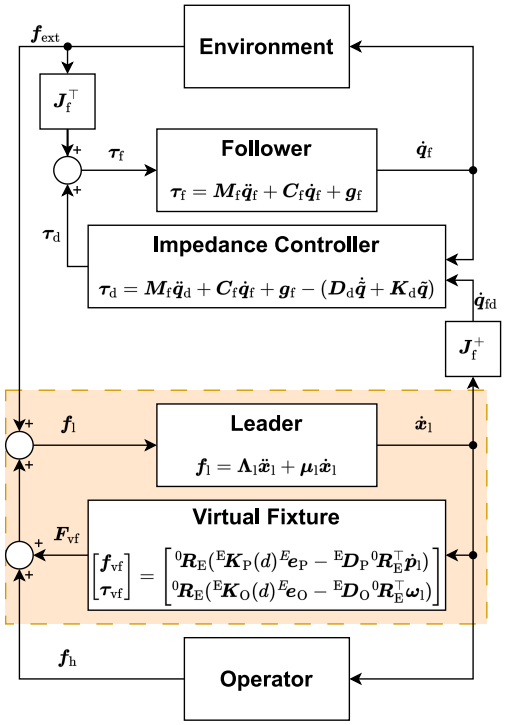

Fig. 1: System representation of the telemanipulation setup. The upper part shows the follower with its impedance controller and the interacting environment. Further, the leader device with the virtual fixture approach and the acting operator is shown. The orange box marks the subsystem that is considered for the stability analysis.

Our contributions are as follows: (1) We improve our previously proposed approach [1] by adding a position fixture to the already existing orientation component. This results in a full 6D guidance that allows the operator to move easily along an ideal insertion vector. (2) We introduce a position dependent variable stiffness to increase the smoothness of the guidance while approaching the nostril. (3) We prove the stability of this variable guidance by introducing suitable energy tanks to ensure the overall passivity of the system.

Experiments show that the improvements of this approach further increase the task performance while reducing the task execution time and interaction force.

[1]The authors are with the Robotics and Human-Machine Interaction Lab at Chemnitz University of Technology, 09126 SN Chemnitz, Germany. Emails: {stephan-andreas.schwarz, ulrike.thomas}@etit.tu-chemnitz.de}

II. RELATED WORK

Telemedicine received a lot of attention within the last decades. From first surgical telemanipulation setups, like AESOP® and ZEUS® [2], the systems improved and were extended rapidly. The da Vinci Surgical System [3] and the DLR MIRO [4] robot are nowadays used for many medical applications. Telepresence and telemanipulation is further increasingly used in healthcare [5].

In many of these interventions it is crucial to avoid undesired contacts with tissue or the tools themselves. This demands for high precision during execution that often results in high mental workload for the operator. To overcome this issue, the concept of virtual fixtures is introduced in telemanipulation [6]. Applying simulated forces and torques either guides the operator towards a desired pose or away from a forbidden region [7]. This concept is already used in medical applications for, e.g., tool collision avoidance [8], optimal needle grasping [9] and workspace limitations [10].

Insertion task like endoscopy, needle insertion or swab samplings are also common in medical applications. Previous works related to performing these task telemanipulated utilize virtual fixtures to increase the safety during the operation. The authors of [11] present a oropharyngeal swab robot that splits the task in a global positioning and a local sampling part. The soft wrist and gripper is positioned using a three degree-of-freedom (DOF) remote center of motion platform. The active gripper then performs the sampling. Forbidden region virtual fixtures are selected manually by the operator based on a 2D image of the throat to avoid undesired contacts with tissue. An implicit neural field is used in [12] for endoscopy to avoid tissue contact while inside narrow workspaces. They use computer tomography (CT) to receive the volume data of the cavity region. From this, the gradient of the distance field is used to adjust the position of the rigid endoscope accordingly.

Our work differs from the presented approaches in several ways. First, our 7 DOF follower can perform the complete insertion task without the need of separating it in a positioning and sampling component. Further, we use online vision-based virtual fixtures instead of manually selected ones. For this, image data from an attached camera are used, so no CT scan is needed for the procedure. Finally, we combine our variable virtual fixture with 6 DOF force feedback to optimize safety, smoothness and task execution time.

The authors of [13] adjust the strength of the fixture by utilizing attached electromyography sensors to increase adaptability to changes in the environment. They ensure stability by allowing control gains only in a reasonable range.

In this work, we adjust the stiffness of the fixtures dependent on the distance to the nostril of the subject. This increases the smoothness of the fixture during the approach. Further, we ensure stability of the system by using passivity theory. Since the increase of stiffness within the virtual fixture induces energy into the system in a similar way as during variable impedance control, we apply a similar passivization strategy as already presented in the literature [14][15][16].

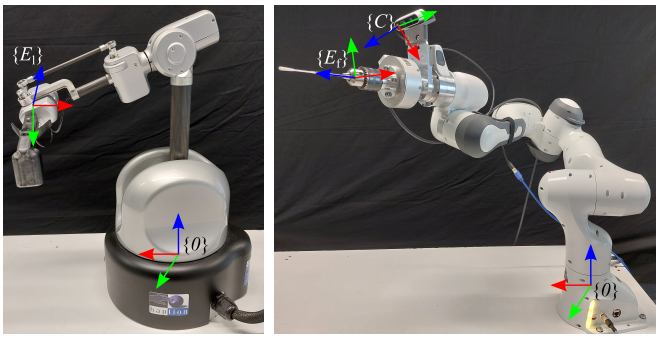

Fig. 2: Telemanipulation setup consisting of the leader device (left) and the follower robot with the attached FT sensor, RGB-D camera and flange (right). The reference frames used are presented with $\boldsymbol{x}$ in red, $\boldsymbol{y}$ in green and $\boldsymbol{z}$ in blue.

Using energy tanks enables the system to become partially active, while still maintaining overall passivity. Unlike other works, we split the position and orientation component into two separate tanks to avoid seemingly unstable behavior due to interactions between the position and orientation fixture.

III. NOMENCLATURE

In the first step, we define the nomenclature and our used reference systems as they are presented in Fig. 2. We use a world frame $\{0\}$ that exists once each at the leader and follower side and is fixed at the robot's bases. Further, each robot has its end effector frame $\{E_{\mathrm{l/f}}\}$ that is positioned at the corresponding end effector. During system initialization, $\{E_{\mathrm{l}}\}$ is aligned to $\{E_{\mathrm{f}}\}$ so that we can unite these frames to $\{E_{\mathrm{l}}\} = \{E_{\mathrm{f}}\} = \{E\}$. Finally, the camera frame $\{C\}$ is of importance for the image processing. It is attached to the RGB lens of the mounted camera.

Each vector is represented with relation to a reference frame. ${}^{E}\boldsymbol{p}$ is thus expressed relative to the end effector frame. The superscripts for vectors expressed in the world frame are omitted for the sake of clarity.

IV. SYSTEM ARCHITECTURE

Our telemanipulation setup is shown in Fig. 2. On the leader side, a Haption Virtuose 6D input device is used. The leader is controlled using the internal, gravity-compensating force controller. Since it is a Cartesian controller and the fixtures are also applied in Cartesian space, we consider the dynamics of the leader robot with

$$\boldsymbol{f}_{\mathrm{l}} = \boldsymbol{f}_{\mathrm{ext}} + \boldsymbol{f}_{\mathrm{h}} + \boldsymbol{F}_{\mathrm{vf}} = \boldsymbol{\Lambda}_{\mathrm{l}}(\boldsymbol{x}_{\mathrm{l}})\ddot{\boldsymbol{x}}_{\mathrm{l}} + \boldsymbol{\mu}_{\mathrm{l}}(\boldsymbol{x}_{\mathrm{l}}, \dot{\boldsymbol{x}}_{\mathrm{l}})\dot{\boldsymbol{x}}_{\mathrm{l}} \qquad (1)$$

also in Cartesian space as proposed in [17]. Note that the robot still consists of rotational joints. $\boldsymbol{f}_{\mathrm{l}}$ describes the total acting forces on the leader device and consists of the feedback force acting on the end effector of the follower $\boldsymbol{f}_{\mathrm{ext}}$, the force applied by the operator $\boldsymbol{f}_{\mathrm{h}}$ and the force generated by the virtual guidance $\boldsymbol{F}_{\mathrm{vf}}$. The latter is capitalized to avoid ambiguity. $\boldsymbol{\Lambda}_{\mathrm{l}}$ and $\boldsymbol{\mu}_{\mathrm{l}}$ describe the robot's inertia and Coriolis and centrifugal matrix expressed in Cartesian space. $\boldsymbol{x}_{\mathrm{l}}$ is the end effector position of the leader device.

The follower consists of a Franka Emika Panda robot together with a mounted 6D force-torque (FT) sensor and a RGB-D camera. A flange is used to hold the swab for the sampling task. In this work, the joint-space impedance controller from our previous work [15] controls the follower. The dynamics of the follower as well as the used control approach are described by

$$\boldsymbol{\tau}_{\mathrm{f}} = \boldsymbol{\tau}_{\mathrm{d}} + \boldsymbol{J}_{\mathrm{f}}^{\top} \boldsymbol{f}_{\mathrm{ext}} = \boldsymbol{M}_{\mathrm{f}}(\boldsymbol{q}_{\mathrm{f}})\ddot{\boldsymbol{q}}_{\mathrm{f}} + \boldsymbol{C}_{\mathrm{f}}(\boldsymbol{q}_{\mathrm{f}}, \dot{\boldsymbol{q}}_{\mathrm{f}})\dot{\boldsymbol{q}}_{\mathrm{f}} + \boldsymbol{g}_{\mathrm{f}}(\boldsymbol{q}_{\mathrm{f}}) \quad (2)$$

$$\boldsymbol{\tau}_{\mathrm{d}} = \boldsymbol{M}_{\mathrm{f}}(\boldsymbol{q}_{\mathrm{f}})\ddot{\boldsymbol{q}}_{\mathrm{d}} + \boldsymbol{C}_{\mathrm{f}}(\boldsymbol{q}_{\mathrm{f}}, \dot{\boldsymbol{q}}_{\mathrm{f}})\dot{\boldsymbol{q}}_{\mathrm{f}} + \boldsymbol{g}_{\mathrm{f}}(\boldsymbol{q}_{\mathrm{f}}) - (\boldsymbol{D}_{\mathrm{d}}\dot{\tilde{\boldsymbol{q}}} + \boldsymbol{K}_{\mathrm{d}}\tilde{\boldsymbol{q}}). \quad (3)$$

$\boldsymbol{\tau}_{\mathrm{f}}$ being the total acting torques on the follower robot, $\boldsymbol{\tau}_{\mathrm{d}}$ the control input from the impedance controller and $\boldsymbol{J}_{\mathrm{f}}$ the end effector Jacobian of the follower. $\boldsymbol{M}_{\mathrm{f}}$, $\boldsymbol{C}_{\mathrm{f}}$ and $\boldsymbol{g}_{\mathrm{f}}$ are the robot's inertia, Coriolis and centrifugal matrix and gravity vector. Finally, $\boldsymbol{D}_{\mathrm{d}}$ and $\boldsymbol{K}_{\mathrm{d}}$ are the desired damping and stiffness of the impedance controller. The controller uses the joint error $\tilde{\boldsymbol{q}} = \boldsymbol{q}_{\mathrm{f}} - \boldsymbol{q}_{\mathrm{fd}}$ between the joint configuration of the follower $\boldsymbol{q}_{\mathrm{f}}$ and the desired configuration $\boldsymbol{q}_{\mathrm{fd}}$, received from the leader, as input. For detailed explanations of the impedance parameter, please refer to [15].

The mounted FT sensor is used to apply the interaction force that is acting on the end effector onto the leader device. We apply our proposed neural network based calibration method to achieve precise measurements during the operation [18]. In the following, we present the image processing that is needed for the guided swab sampling and the virtual fixture algorithm. The algorithm is described in general and can be applied to both nostril in the same way.

A. Image Processing

The RGB images from the camera are used to estimate a 2D face mesh of the person standing in front of the robot. The Google MediaPipe library [19] is utilized to compute the 478 landmarks of the face as shown in Fig. 3a. Two components are necessary to realize the proposed virtual guidance, the nostril position $\boldsymbol{p}_{\mathrm{N}}$ and the ideal insertion vector $\boldsymbol{p}_{\mathrm{in}}$. Averaging the 4 landmark values around the nostril results in a good estimation of the nostril position in the image plane. Together with the depth data from the depth image, the nostril position relative to the camera frame ${}^{C}\boldsymbol{p}_{\mathrm{N}}$ can be computed.

The orientation of the head is computed using the opencv PNP solver [20] and suitable landmarks of the face mesh. ${}^{C}\boldsymbol{p}_{\mathrm{in}}$ can be computed by applying a fixed rotation on the estimated head orientation. This fixed rotation was experimentally estimated using the dummy shown in Fig. 3a. The nostril position and insertion vector are shown in blue and green, respectively. The calibration method from [21] provides us with the homogeneous transformation ${}^{E}\boldsymbol{T}_{C}$, with which we receive the nostril position and insertion vector with respect to the end effector frame.

B. Variable Virtual Guidance

In this work, we extend our already proposed virtual guidance approach [1] by two aspects. First, we add a position fixture to receive full 6D guidance and secondly, we adjust our fixture stiffness depending on the distance of the end effector to the subject to increase the usability of the system. We apply this approach on a nasopharyngeal swab sampling task, but it can be easily adapted for other insertion tasks. Fig. 3b shows the general concept of the fixture. For the sake of completeness, we give a short summary of the orientation fixture.

1) Orientation Fixture: The goal of this component is to bring the end effector in an orientation in which it aims towards the nostril. This means, the $\boldsymbol{z}_{\mathrm{E}}$ axis has to be aligned with the nostril vector ${}^{E}\boldsymbol{p}_{\mathrm{N}}$. Starting from the angle $\boldsymbol{\theta}$ and unit vector ${}^{E}\boldsymbol{e}$ of the angle axis between ${}^{E}\boldsymbol{z}_{\mathrm{E}}$ and ${}^{E}\boldsymbol{p}_{\mathrm{N}}$, we can define the orientation error as the vector component of the resulting quaternion given with

$${}^{E}\boldsymbol{e}_{\mathrm{O}} = {}^{E}\boldsymbol{e} \sin\frac{\theta}{2} = \frac{{}^{E}\boldsymbol{z}_{\mathrm{E}} \times {}^{E}\boldsymbol{p}_{\mathrm{N}}}{\|{}^{E}\boldsymbol{z}_{\mathrm{E}}\| \|{}^{E}\boldsymbol{p}_{\mathrm{N}}\| \sin\theta} \sin\frac{\theta}{2} \quad (4)$$

$$\theta = \arccos \frac{{}^{E}\boldsymbol{z}_{\mathrm{E}} \cdot {}^{E}\boldsymbol{p}_{\mathrm{N}}}{\|{}^{E}\boldsymbol{z}_{\mathrm{E}}\| \|{}^{E}\boldsymbol{p}_{\mathrm{N}}\|} \ . \quad (5)$$

Adding the additional damping based on the angular velocity $\boldsymbol{\omega}_{\mathrm{l}}$, the Cartesian virtual torque $\boldsymbol{\tau}_{\mathrm{vf}}$ is defined by

$$\boldsymbol{\tau}_{\mathrm{vf}} = {}^{0}\boldsymbol{R}_{E} \left({}^{E}\boldsymbol{K}_{\mathrm{O}}(d)\, {}^{E}\boldsymbol{e}_{\mathrm{O}} - {}^{E}\boldsymbol{D}_{\mathrm{O}}\, {}^{0}\boldsymbol{R}_{E}^{\mathsf{T}}\, \boldsymbol{\omega}_{\mathrm{l}} \right) \ . \quad (6)$$

Note that against [1], the proportional gain ${}^{E}\boldsymbol{K}_{\mathrm{O}}(d)$ now depends on the distance towards the nostril, defined with $d = \|{}^{E}\boldsymbol{p}_{\mathrm{N}}\|$ and $\|\cdot\|$ being the Euclidean norm of the vector.

2) Position Fixture: The goal of the position fixture is twofold. First, the end effector should be positioned along the estimated insertion vector $\boldsymbol{p}_{\mathrm{in}}$. As shown in Fig. 3b, this position error can be defined with

$${}^{E}\boldsymbol{e}_{\mathrm{P1}} = {}^{E}\boldsymbol{p}_{\mathrm{N}} + d\, {}^{E}\boldsymbol{p}_{\mathrm{in}} \quad (7)$$

since $\|\boldsymbol{p}_{\mathrm{in}}\| = 1$ is a unit vector. This error drags the end effector towards the insertion line. Together with the orientation fixture, the swab aligns with the insertion vector, pointing towards the nostril.

Secondly, it is desirable to prevent an insertion too deep into the nostril to avoid any potential damage on the subject. For this, an additional component is added when the distance falls under a lower threshold. This error is defined with

$${}^{E}\boldsymbol{e}_{\mathrm{P2}} = \begin{cases} \begin{bmatrix} 0 & 0 & (d - d_{\min}) \end{bmatrix}^{\top} & , d < d_{\min} \\ \begin{bmatrix} 0 & 0 & 0 \end{bmatrix}^{\top} & , \text{else} \end{cases} . \quad (8)$$

The resulting force can be computed with

$$\boldsymbol{f}_{\mathrm{vf}} = {}^{0}\boldsymbol{R}_{E} \left(\begin{bmatrix} {}^{E}\boldsymbol{K}_{\mathrm{P1}}(d)\, {}^{E}\boldsymbol{K}_{\mathrm{P2}} \end{bmatrix} \begin{bmatrix} {}^{E}\boldsymbol{e}_{\mathrm{P1}}^{\top} & {}^{E}\boldsymbol{e}_{\mathrm{P2}}^{\top} \end{bmatrix}^{\top} - {}^{E}\boldsymbol{D}_{\mathrm{P}}\, {}^{0}\boldsymbol{R}_{E}^{\top} \dot{\boldsymbol{p}}_{\mathrm{l}} \right) \quad (9)$$

$$\boldsymbol{f}_{\mathrm{vf}} = {}^{0}\boldsymbol{R}_{E} \left({}^{E}\boldsymbol{K}_{\mathrm{P}}(d) {}^{E}\boldsymbol{e}_{\mathrm{P}} - {}^{E}\boldsymbol{D}_{\mathrm{P}}\, {}^{0}\boldsymbol{R}_{E}^{\top} \dot{\boldsymbol{p}}_{\mathrm{l}} \right) \ . \quad (10)$$

$\{{}^{E}\boldsymbol{K}_{\mathrm{P1}}, {}^{E}\boldsymbol{K}_{\mathrm{P2}}, {}^{E}\boldsymbol{D}_{\mathrm{P}}\} \in \mathbb{R}^{3\times3}$ are the positive semi-definite diagonal matrices describing the gains of the proportional and derivative parts of the fixture. ${}^{E}\boldsymbol{K}_{\mathrm{P1}}$ depends again on the distance d towards the nostril. ${}^{E}\boldsymbol{e}_{\mathrm{P1}}$ and ${}^{E}\boldsymbol{e}_{\mathrm{P2}}$ were separated to enable a stiffer fixture regarding the insertion depth compared the alignment with the insertion vector.

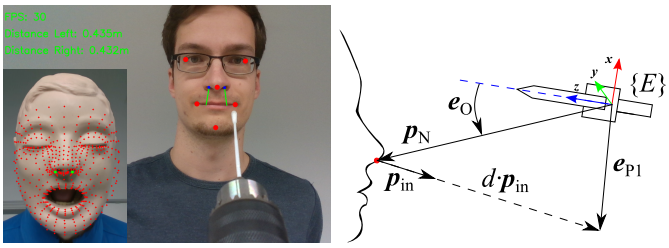

(a) Face Detection (b) Virtual Fixture

Fig. 3: (a) Face detection algorithm with face mesh (dummy - red), used landmarks for PNP solver (red), nostril position (blue) and insertion vector (green). (b) Representation of the position and orientation error to align the swab with the insertion vector $\boldsymbol{p}_{\text{in}}$ pointing towards the nostril $\boldsymbol{p}_{\text{N}}$.

With this, we receive a full 6D virtual fixture to guide the operator towards the nostril that also avoids dangerous penetration depths. The fixtures, depending on the distance d towards the nostril, can be combined into

$$\boldsymbol{F}_{\text{vf}} = \begin{bmatrix} \boldsymbol{f}_{\text{vf}} \\ \boldsymbol{\tau}_{\text{vf}} \end{bmatrix} = \begin{bmatrix} {}^{0}\boldsymbol{R}_{\text{E}}({}^{E}\boldsymbol{K}_{\text{P}}(d)\,{}^{E}\boldsymbol{e}_{\text{P}} - {}^{E}\boldsymbol{D}_{\text{P}}\,{}^{0}\boldsymbol{R}_{\text{E}}^{\top}\dot{\boldsymbol{p}}_{\text{l}}) \\ {}^{0}\boldsymbol{R}_{\text{E}}({}^{E}\boldsymbol{K}_{\text{O}}(d)\,{}^{E}\boldsymbol{e}_{\text{O}} - {}^{E}\boldsymbol{D}_{\text{O}}\,{}^{0}\boldsymbol{R}_{\text{E}}^{\top}\boldsymbol{\omega}_{\text{l}}) \end{bmatrix} . \quad (11)$$

3) Position Dependency: A linear relationship between the proportional gains and the distance of the end effector towards the nostril is used. Let $k_i(d)$ with $i \in \{\text{O}, \text{P1}\}$ be the diagonal element related to the corresponding diagonal matrix ${}^{E}\boldsymbol{K}_i$, then the gain can be defined with

$$k_i(d) = \begin{cases} \underline{k}_i & , \overline{d} < d \\ \underline{k}_i + \frac{\overline{k}_i - \underline{k}_i}{\underline{d} - \overline{d}}(d - \overline{d}) & , \underline{d} < d \leq \overline{d} \\ \overline{k}_i & , d \leq \underline{d} \end{cases} , \quad (12)$$

and $\{\overline{a}, \underline{a}\} \geq 0$ for $a \in \{d, k_i\}$ being the upper and lower limit of the distance and gain value, respectively.

V. STABILITY ANALYSIS

Passivity theory is used to analyze and ensure the stability of the telemanipulation system. In our previous work [15], the passivity of the follower robot and the impedance controller is already shown. Furthermore, the environment and the operator are assumed to be passive. Since the interconnection of passive subsystems implies the passivity of the complete system [22], we evaluate the passivity of the leader robot and the virtual fixture element. The orange box in Fig. 1 shows the relevant subsystem. Considering the input-output pair $((\boldsymbol{f}_{\text{h}} + \boldsymbol{f}_{\text{ext}}), \dot{\boldsymbol{x}}_{\text{l}})$, we can define our Ljapunow candidate with

$$\mathcal{V}(\boldsymbol{x}_{\text{l}}, \dot{\boldsymbol{x}}_{\text{l}}) = \frac{1}{2}\dot{\boldsymbol{x}}_{\text{l}}^{\top}\boldsymbol{\Lambda}_{\text{l}}\dot{\boldsymbol{x}}_{\text{l}} + \frac{1}{2}\boldsymbol{e}_{\text{P}}^{\top}\boldsymbol{K}_{\text{P}}(d)\boldsymbol{e}_{\text{P}} + \frac{1}{2}\boldsymbol{e}_{\text{O}}^{\top}\boldsymbol{K}_{\text{O}}(d)\boldsymbol{e}_{\text{O}} \quad (13)$$

being the kinetic energy of the leader and the stored energy in the virtual fixture consisting of the position and orientation component. Note, that the potential energy of the leader is omitted due to its internal gravity compensation. Since $\boldsymbol{\Lambda}_{\text{l}}$ is positive definite by default and according to (12) $\boldsymbol{K}_{\text{P}}$ and $\boldsymbol{K}_{\text{O}}$ are positive semi-definite, $\mathcal{V} \geq 0$ is given. The passivity of this subsystem is thus guaranteed, if the following condition holds for all possible system configurations and $t \in \mathbb{R}_0^+$.

$$\mathcal{V}(t) - \mathcal{V}(0) \leq \int_0^t \dot{\boldsymbol{x}}_{\text{l}}(\tau)^{\top}(\boldsymbol{f}_{\text{ext}}(\tau) + \boldsymbol{f}_{\text{h}}(\tau))\mathrm{d}\tau \quad (14)$$

Differentiate this results in

$$\dot{\mathcal{V}} \leq \dot{\boldsymbol{x}}_{\text{l}}^{\top}(\boldsymbol{f}_{\text{ext}} + \boldsymbol{f}_{\text{h}}) \quad (15)$$

which has to be valid to ensure passivity and thus stability. Computing the derivative of (13) gives

$$\dot{\mathcal{V}} = \dot{\boldsymbol{x}}_{\text{l}}^{\top}\boldsymbol{\Lambda}_{\text{l}}\ddot{\boldsymbol{x}}_{\text{l}} + \frac{1}{2}\dot{\boldsymbol{x}}_{\text{l}}^{\top}\dot{\boldsymbol{\Lambda}}_{\text{l}}\dot{\boldsymbol{x}}_{\text{l}} + \boldsymbol{e}_{\text{P}}^{\top}\boldsymbol{K}_{\text{P}}\dot{\boldsymbol{e}}_{\text{P}} + \frac{1}{2}\boldsymbol{e}_{\text{P}}^{\top}\dot{\boldsymbol{K}}_{\text{P}}\boldsymbol{e}_{\text{P}} + \boldsymbol{e}_{\text{O}}^{\top}\boldsymbol{K}_{\text{O}}\dot{\boldsymbol{e}}_{\text{O}} + \frac{1}{2}\boldsymbol{e}_{\text{O}}^{\top}\dot{\boldsymbol{K}}_{\text{O}}\boldsymbol{e}_{\text{O}} . \quad (16)$$

Computing $\boldsymbol{\Lambda}_{\text{l}}\ddot{\boldsymbol{x}}_{\text{l}}$ from (1) and using the skew-symmetric characteristic $(\dot{\boldsymbol{\Lambda}}_{\text{l}} - 2\boldsymbol{\mu}_{\text{l}}) = 0$, we obtain

$$\dot{\mathcal{V}} = \dot{\boldsymbol{x}}_{\text{l}}^{\top}(\boldsymbol{f}_{\text{ext}} + \boldsymbol{f}_{\text{h}}) + \dot{\boldsymbol{x}}_{\text{l}}^{\top}\boldsymbol{F}_{\text{vf}} + \boldsymbol{e}_{\text{P}}^{\top}\boldsymbol{K}_{\text{P}}\dot{\boldsymbol{e}}_{\text{P}} + \frac{1}{2}\boldsymbol{e}_{\text{P}}^{\top}\dot{\boldsymbol{K}}_{\text{P}}\boldsymbol{e}_{\text{P}} + \boldsymbol{e}_{\text{O}}^{\top}\boldsymbol{K}_{\text{O}}\dot{\boldsymbol{e}}_{\text{O}} + \frac{1}{2}\boldsymbol{e}_{\text{O}}^{\top}\dot{\boldsymbol{K}}_{\text{O}}\boldsymbol{e}_{\text{O}} . \quad (17)$$

Assuming that the nostril position is constant, we can simplify $\dot{\boldsymbol{e}}_{\text{P}} = -\dot{\boldsymbol{p}}_{\text{l}}$ and $\dot{\boldsymbol{e}}_{\text{O}} = -\boldsymbol{\omega}_{\text{l}}$. With $\dot{\boldsymbol{x}}_{\text{l}}^{\top} = \begin{bmatrix} \dot{\boldsymbol{p}}_{\text{l}}^{\top} & \boldsymbol{\omega}_{\text{l}}^{\top} \end{bmatrix}$ and $\boldsymbol{F}_{\text{vf}}$ from (11) the deviation of the Ljapunow candidate and thus the passivity condition are given with

$$\dot{\mathcal{V}} = \dot{\boldsymbol{x}}_{\text{l}}^{\top}(\boldsymbol{f}_{\text{ext}} + \boldsymbol{f}_{\text{h}}) - \dot{\boldsymbol{p}}_{\text{l}}^{\top}\boldsymbol{D}_{\text{P}}\dot{\boldsymbol{p}}_{\text{l}} + \frac{1}{2}\boldsymbol{e}_{\text{P}}^{\top}\dot{\boldsymbol{K}}_{\text{P}}\boldsymbol{e}_{\text{P}} - \boldsymbol{\omega}_{\text{l}}^{\top}\boldsymbol{D}_{\text{O}}\boldsymbol{\omega}_{\text{l}} + \frac{1}{2}\boldsymbol{e}_{\text{O}}^{\top}\dot{\boldsymbol{K}}_{\text{O}}\boldsymbol{e}_{\text{O}} \quad (18)$$

$$-\dot{\boldsymbol{p}}_{\text{l}}^{\top}\boldsymbol{D}_{\text{P}}\dot{\boldsymbol{p}}_{\text{l}} + \frac{1}{2}\boldsymbol{e}_{\text{P}}^{\top}\dot{\boldsymbol{K}}_{\text{P}}\boldsymbol{e}_{\text{P}} - \boldsymbol{\omega}_{\text{l}}^{\top}\boldsymbol{D}_{\text{O}}\boldsymbol{\omega}_{\text{l}} + \frac{1}{2}\boldsymbol{e}_{\text{O}}^{\top}\dot{\boldsymbol{K}}_{\text{O}}\boldsymbol{e}_{\text{O}} \leq 0 . \quad (19)$$

It can be seen that the damping components of the virtual fixture dissipate energy. Yet, changes of the stiffness values induce and dissipate energy into the system whenever the corresponding stiffness increases or decreases. This might violate the passivity condition and thus, global asymptotic stability is not guaranteed.

As already presented in [14] and [16], an energy tank can be introduced to track the amount of dissipated energy to allow partially active behavior while maintaining the overall passivity of the system. In this work, energy tanks are also used to maintain stability. In contrast to the mentioned work, we introduce two energy tanks to differentiate between the position and orientation component of the fixture. This results from the different magnitude of the generated energy, which might cause seemingly unstable behavior in one component due to the energy dissipation of the other component.

In the following, the algorithm for the energy tank of the position component is presented. This can directly be applied to the orientation component. The energy tank T_{P} is defined

by the parameter $x_{\mathrm{t_P}}$ describing the level of the tank.

$$\begin{aligned}\dot{x}_{\mathrm{t_P}} &= \frac{\sigma_{1_\mathrm{P}}}{x_{\mathrm{t_P}}}\dot{\boldsymbol{p}}_\mathrm{l}^\top \boldsymbol{D}_\mathrm{P}\dot{\boldsymbol{p}}_\mathrm{l} - \frac{\sigma_{2_\mathrm{P}}}{2x_{\mathrm{t_P}}}\boldsymbol{e}_\mathrm{P}^\top \dot{\boldsymbol{K}}_\mathrm{P}^{'}\boldsymbol{e}_\mathrm{P} \\ T_\mathrm{P} &= \frac{1}{2}x_{\mathrm{t_P}}^2 \\ \dot{T}_\mathrm{P} &= x_{\mathrm{t_P}}\dot{x}_{\mathrm{t_P}} = \sigma_{1_\mathrm{P}}\dot{\boldsymbol{p}}_\mathrm{l}^\top \boldsymbol{D}_\mathrm{P}\dot{\boldsymbol{p}}_\mathrm{l} - \frac{\sigma_{2_\mathrm{P}}}{2}\boldsymbol{e}_\mathrm{P}^\top \dot{\boldsymbol{K}}_\mathrm{P}^{'}\boldsymbol{e}_\mathrm{P}\end{aligned} \tag{20}$$

It can be seen, that the tank is filled by the dissipated energy due to the damping and by the decrease of stiffness. Its level decreases due to the increase of stiffness. $x_{\mathrm{t_P}}(0) > 0$ is defined to avoid singularities. σ_{1_P} and σ_{2_P} bound the upper limit of the energy tank to T_{Pmax} and are given with

$$\begin{aligned}\sigma_{1_\mathrm{P}} &= \begin{cases} 0 & , T_\mathrm{P} \geq T_{\mathrm{Pmax}} \\ 1 & , \text{else} \end{cases}, \\ \sigma_{2_\mathrm{P}} &= \begin{cases} 0 & , T_\mathrm{P} \geq T_{\mathrm{Pmax}} \wedge \dot{\boldsymbol{K}}_\mathrm{P}^{'} < 0 \\ 1 & , \text{else} \end{cases}.\end{aligned} \tag{21}$$

$\dot{\boldsymbol{K}}_\mathrm{P}^{'}$ is the modified change of the stiffness of the virtual fixture component. It contains the modified change of k_{P1} defined with

$$\dot{k}_{\mathrm{P1}}^{'} = \begin{cases} \dot{k}_{\mathrm{P1}} & , \dot{k}_{\mathrm{P1}} \leq 0 \\ 0 & , \dot{k}_{\mathrm{P1}} > 0 \wedge T_\mathrm{P} \leq T_{\mathrm{Pmin}} \\ \dot{k}_{\mathrm{P1}} & , 0 < \dot{k}_{\mathrm{P1}} < \dot{k}_{\mathrm{Pmax}} \wedge T_\mathrm{P} > T_{\mathrm{Pmin}} \\ \dot{k}_{\mathrm{Pmax}} & , \dot{k}_{\mathrm{Pmax}} \leq \dot{k}_{\mathrm{P1}} \wedge T_\mathrm{P} > T_{\mathrm{Pmin}} \end{cases} \tag{22}$$

When the stiffness decreases, no active behavior occurs, thus no limitation is active. When the lower tank limit T_{Pmin} is reached, an increase of the stiffness is prohibited. When the tank contains previously dissipated energy, the stiffness can increase. Yet the increase is limited by an upper value $\dot{k}_{\mathrm{Pmax}}$ that is defined with

$$\dot{k}_{\mathrm{Pmax}} = \min\left(\frac{2(T_\mathrm{P} - T_{\mathrm{Pmin}})}{\Delta t \|\boldsymbol{e}_\mathrm{P}\|}, \dot{k}_{\mathrm{Plim}}\right) . \tag{23}$$

This restricts the stiffness in a way, that it either consumes all stored energy within the next timestep Δt or is bounded by a maximum increase $\dot{k}_{\mathrm{Plim}}$. The upper limit is introduced to avoid a quasi-instantaneous increase of stiffness resulting from the restricting behavior of the energy tank.

Adapting the change of stiffness as described above and adjusting our stability analysis with the two introduced energy tanks results in

$$\mathcal{V}^{'} = \mathcal{V} + T_\mathrm{P} + T_\mathrm{O} \tag{24}$$

$$\begin{aligned}\dot{\mathcal{V}}^{'} = {} & \dot{\boldsymbol{x}}_\mathrm{l}^\top(\boldsymbol{f}_{\mathrm{ext}} + \boldsymbol{f}_\mathrm{h}) - \dot{\boldsymbol{p}}_\mathrm{l}^\top \boldsymbol{D}_\mathrm{P}\dot{\boldsymbol{p}}_\mathrm{l} + \frac{1}{2}\boldsymbol{e}_\mathrm{P}^\top \dot{\boldsymbol{K}}_\mathrm{P}^{'}\boldsymbol{e}_\mathrm{P} \\ & - \boldsymbol{\omega}_\mathrm{l}^\top \boldsymbol{D}_\mathrm{O}\boldsymbol{\omega}_\mathrm{l} + \frac{1}{2}\boldsymbol{e}_\mathrm{O}^\top \dot{\boldsymbol{K}}_\mathrm{O}^{'}\boldsymbol{e}_\mathrm{O} + \sigma_{1_\mathrm{P}}\dot{\boldsymbol{p}}_\mathrm{l}^\top \boldsymbol{D}_\mathrm{P}\dot{\boldsymbol{p}}_\mathrm{l} - \frac{\sigma_{2_\mathrm{P}}}{2}\boldsymbol{e}_\mathrm{P}^\top \dot{\boldsymbol{K}}_\mathrm{P}^{'}\boldsymbol{e}_\mathrm{P} \\ & + \sigma_{1_\mathrm{O}}\boldsymbol{\omega}_\mathrm{l}^\top \boldsymbol{D}_\mathrm{O}\boldsymbol{\omega}_\mathrm{l} - \frac{\sigma_{2_\mathrm{O}}}{2}\boldsymbol{e}_\mathrm{O}^\top \dot{\boldsymbol{K}}_\mathrm{O}^{'}\boldsymbol{e}_\mathrm{O} .\end{aligned} \tag{25}$$

This gives the following passivity condition.

$$\begin{aligned}& (\sigma_{1_\mathrm{P}} - 1)\dot{\boldsymbol{p}}_\mathrm{l}^\top \boldsymbol{D}_\mathrm{P}\dot{\boldsymbol{p}}_\mathrm{l} + \frac{1}{2}(1 - \sigma_{2_\mathrm{P}})\boldsymbol{e}_\mathrm{P}^\top \dot{\boldsymbol{K}}_\mathrm{P}^{'}\boldsymbol{e}_\mathrm{P} \\ & + (\sigma_{1_\mathrm{O}} - 1)\boldsymbol{\omega}_\mathrm{l}^\top \boldsymbol{D}_\mathrm{O}\boldsymbol{\omega}_\mathrm{l} + \frac{1}{2}(1 - \sigma_{2_\mathrm{O}})\boldsymbol{e}_\mathrm{O}^\top \dot{\boldsymbol{K}}_\mathrm{O}^{'}\boldsymbol{e}_\mathrm{O} \leq 0\end{aligned} \tag{26}$$

Since $\sigma_{1_{\mathrm{P/O}}} \in \{0, 1\}$ results in $(\sigma_{1_{\mathrm{P/O}}} - 1) \leq 0$ and $\sigma_{2_{\mathrm{P/O}}} \in \{0, 1\}$ is only 0 when the stiffness decreases, the passivity condition holds. By introducing the two energy tanks, the global asymptotic stability of the considered subsystem is proven and thus, the overall telemanipulation system is stable.

VI. EXPERIMENTS

In this section, we examine our approach on the presented telemanipulation setup. All components run on a single computer using a Linux real-time kernel, C++ and Python. The follower and leader controller run at 1 kHz, the FT sensor at 500 Hz and the image processing at around 25 fps. The used parameters are listed in Tab. I. We select the boundaries for the energy tanks in a way, that makes it possible to generate enough energy during one sampling procedure.

Two experiments are performed in this work. The goal of the first one is to validate the functionality of the proposed virtual guidance and to compare it with the authors previous results, in which only a constant orientation fixture was applied [1]. In this experiment, an expert user was told to perform a single nasopharyngeal swab sampling on the shown dummy. One sampling procedure consists of the following steps. First, bring the swab close to the nostril in a pose that is suitable for the insertion. Secondly, the swab has to be inserted in the nostril. Here, violating a lower limit of $d = 0.2\,\mathrm{m}$ counts as critical failure. After insertion, a small circular motion has to be performed to take the sample. Finally, the swab has to be extracted from the nostril and brought to a position away from the subject. Starting from a position outside of the range of the virtual fixtures, the guidance is supposed to guide the operator towards the desirable configuration while approaching. With active guidance and force feedback, the resulting interaction forces should be lower compared to our previous approach.

In the second experiment, we compare our guided telemanipulation approach with the unguided one. Here, the expert user was told to perform 15 swab samplings with the guidance and 15 without any guidance. In both cases, force feedback is provided to the operator. We compare the task execution times and the acting forces and torques during the sampling. Each single sampling procedure is similar to the one in experiment 1. For the task execution time, the task

TABLE I: Parameters of the virtual fixtures.

Parameter	Value	Parameter	Value
$d_{\mathrm{O_{x,y}}}$	$0.1\,\mathrm{Nm/(rad\,s^{-1})}$	$d_{\mathrm{P_{x,y,z}}}$	$1.5\,\mathrm{N/(m\,s^{-1})}$
$d_{\mathrm{O_z}}$	$0\,\mathrm{Nm/(rad\,s^{-1})}$	$\underline{k}_{\mathrm{P1_{x,y,z}}}$	$0\,\mathrm{N/m}$
$\underline{k}_{\mathrm{O_{x,y,z}}}$	$0\,\mathrm{Nm}$	$\overline{k}_{\mathrm{P1_{x,y,z}}}$	$22.5\,\mathrm{N/m}$
$\overline{k}_{\mathrm{O_{x,y}}}$	$3.5\,\mathrm{Nm}$	$k_{\mathrm{P2_{x,y}}}$	$0\,\mathrm{N/m}$
$\overline{k}_{\mathrm{O_z}}$	$0\,\mathrm{Nm}$	$k_{\mathrm{P2_z}}$	$100\,\mathrm{N/m}$
T_{Omax}	$0.15\,\mathrm{J}^2$	T_{Pmax}	$2.5\,\mathrm{J}^2$
T_{Omin}	$0.1\,\mathrm{J}^2$	T_{Pmin}	$1.5\,\mathrm{J}^2$
$T_\mathrm{O}(0)$	$0.125\,\mathrm{J}^2$	$T_\mathrm{P}(0)$	$2.0\,\mathrm{J}^2$
$\dot{k}_{\mathrm{Olim}}$	$10\,\mathrm{Nm/(rad\,s)}$	$\dot{k}_{\mathrm{Plim}}$	$50\,\mathrm{N/(m\,s)}$
$\underline{d}$	$0.3\,\mathrm{m}$	$\overline{d}$	$0.4\,\mathrm{m}$
d_{min}	$0.25\,\mathrm{m}$		

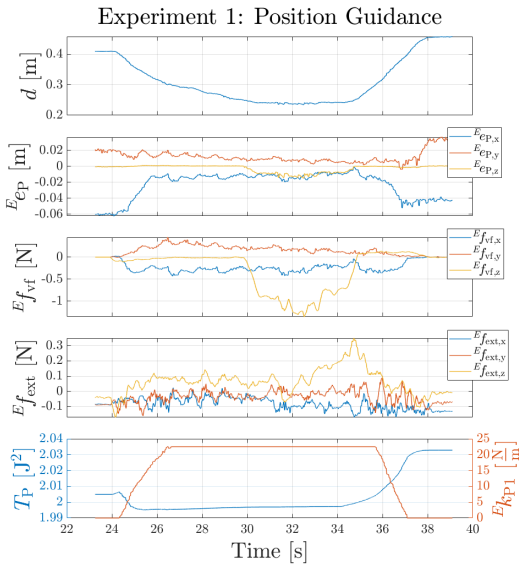

Fig. 4: Experiment 1: Distance d, position error ${}^{E}\boldsymbol{e}_{\mathrm{P}}$ with resulting virtual force ${}^{E}\boldsymbol{f}_{\mathrm{vf}}$, external force ${}^{E}\boldsymbol{f}_{\mathrm{ext}}$ and the stored energy in the tank T_{P} with the acting stiffness ${}^{E}k_{\mathrm{P1}}$ of the position component during the guided sampling.

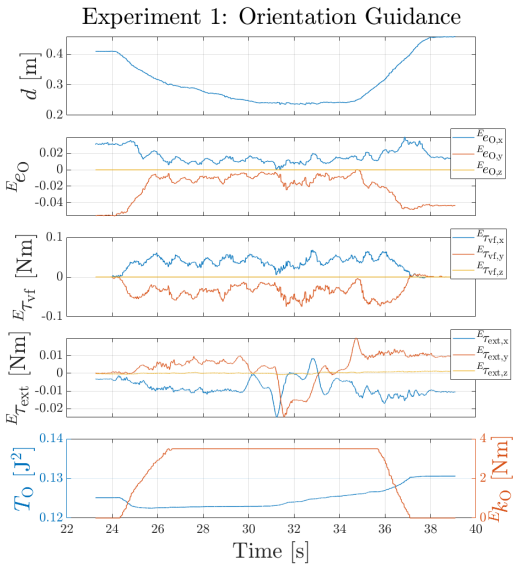

Fig. 5: Experiment 1: Distance d, orientation error ${}^{E}\boldsymbol{e}_{\mathrm{O}}$ with resulting virtual torque ${}^{E}\boldsymbol{\tau}_{\mathrm{vf}}$, external torque ${}^{E}\boldsymbol{\tau}_{\mathrm{ext}}$ and the stored energy in the tank T_{O} with the acting stiffness ${}^{E}k_{\mathrm{O}}$ of the orientation component during the guided sampling.

starts, when the end effector enters the $0.4\,\mathrm{m}$ range towards the patient and finishes when it is again over $0.4\,\mathrm{m}$ away from the patient. We consider the parts of the motion where the robot is closer than $0.28\,\mathrm{m}$ to the nostril for the comparison of the acting forces and torques. At this distance, the end of the swab is positioned directly in front the nostril and contacts can occur. We expect shorter task execution time, lower interaction forces and more intuitive swab insertion reported by the user while having the guidance active.

VII. RESULTS

Fig. 4 and 5 show the results of the first experiment. It can be seen that the errors are reduced due to the fixtures. Further, the added error ${}^{E}\boldsymbol{e}_{\mathrm{P2}}$ hinders the operator from inserting the swab deeper than $0.25\,\mathrm{m}$. The increase and decrease of the stiffness values during the sample are shown which results in the presented values of the energy tanks T_i. During the whole sample, more energy was dissipated then generated. This is consistent with our approach, since the damping dissipates energy during the whole motion and the stiffness once increases and once decreases. Assuming similar error during these motions, the changes in stiffness compensate each other. Even if this experiment shows passive behavior during the sampling procedure, it is advisable to use the proposed energy tanks to ensure stability independent of the specific experiment. The maximum external force is with $0.3495\,\mathrm{N}$ more than twice as low compared to our previous approach, where the maximum force was around $0.9\,\mathrm{N}$. Same for the external torques, that where reduced from $0.1\,\mathrm{Nm}$ to $0.0249\,\mathrm{Nm}$. Further, the interactions during the rotation in the nostril are well visible. Due to the active fixtures this motion is constrained which reduces the resulting interaction force and torque.

The results of the second experiment are shown in Table II. As expected, the mean task execution time and interaction force and torque are smaller while using the guidance. The operator also mentioned that less attention was needed to insert the swab correctly into the nostril. Fig. 6 shows the resulting forces and torques again in two box plots. Besides reducing the mean forces and torques, these plots show additional improvements due to the guidance. Regarding the force, it can be seen that due to the guidance nearly no outliers occurred. Thus the fixture improves the safety of the sampling. Further, the outliers in torque are similar compared to free telemanipulation. This results from the demanded circular motion to take the sample. Considering the much smaller variance of the torques, we can assume that the outliers occur during the circular motion and nearly no outliers appear during insertion and extraction.

VIII. CONCLUSIONS

This paper presents a position dependent virtual guidance approach to perform insertion tasks with nasopharyngeal swab samplings as use case. It extends the authors' previous

TABLE II: Experiment 2: Mean value, variance and maximum value of the task execution time and interaction force and torque during the 15 guided and unguided samplings.

		$\overline{(\cdot)}$	$\sigma(\cdot)$	$(\cdot)_{\max}$
guided	t_{task}	$11.7575\,\mathrm{s}$	$2.3161\,\mathrm{s}$	$17.5290\,\mathrm{s}$
	$\|\boldsymbol{f}_{\mathrm{ext}}\|$	$0.3255\,\mathrm{N}$	$0.1090\,\mathrm{N}$	$0.6446\,\mathrm{N}$
	$\|\boldsymbol{\tau}_{\mathrm{ext}}\|$	$0.0126\,\mathrm{N\,m}$	$0.0098\,\mathrm{N\,m}$	$0.0817\,\mathrm{N\,m}$
unguided	t_{task}	$13.1537\,\mathrm{s}$	$1.9112\,\mathrm{s}$	$15.8610\,\mathrm{s}$
	$\|\boldsymbol{f}_{\mathrm{ext}}\|$	$0.5228\,\mathrm{N}$	$0.1253\,\mathrm{N}$	$1.0337\,\mathrm{N}$
	$\|\boldsymbol{\tau}_{\mathrm{ext}}\|$	$0.0188\,\mathrm{N\,m}$	$0.0158\,\mathrm{N\,m}$	$0.0795\,\mathrm{N\,m}$

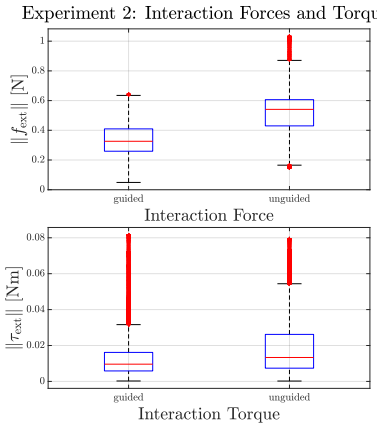

Fig. 6: Experiment 2: Boxplots of the interactions forces and torques during the 15 guided and unguided samplings.

approach by a position fixture, designing the stiffness to be position dependent and proving the stability of the system.

RGB-D data are used to detect the position of the nostril as well as an ideal insertion vector to align the end effector to. Applying a spring-damper based virtual fixture enables the system to guide the operator towards a desirable pose for the swab insertion. Using stiffness values that depend on the distance towards the nostril increases the smoothness of the sampling procedure. A stability analysis has been presented to prove the passivity of the system by introducing two energy tanks that restrict potentially active behavior. Experiments have been conducted using a physical telemanipulation system and a human dummy. Combining the extended virtual fixtures with 6D force feedback improves the task performance compared to the authors' previous approach. Further, a comparison between guided and unguided sampling has been performed by an expert user. The results show improvements in task execution time and interaction force and torque.

Future works aim at making the approach more robust. Especially the vision-based target pose detection is sensitive to changing light conditions. Finally, a user study will be conducted to validate the improvements not only by one single trained operator but a significant number of trained and untrained subjects.

ACKNOWLEDGMENT

This project was founded by the Deutsche Forschungsgemeinschaft (DFG, German Research Foundation) - Project-ID 416228727 - SFB 1410.

REFERENCES

[1] S. A. Schwarz and U. Thomas, "Vision-based Shared Control for Telemanipulated Nasopharyngeal Swab Sampling," in 2023 International Symposium on Medical Robotics (ISMR), pp. 1–7 May 2023.

[2] F. Pugin, P. Bucher and P. Morel, "History of robotic surgery: from AESOP® and ZEUS® to da Vinci®," in Journal of Visceral Surgery, vol. 148(5 Suppl), pp. e3–e8., October 2011.

[3] 2024 Intuitive Surgical, "The da Vinci surgical system," accessed on 21st February 2024 at https://www.intuitive.com/en-us/patients/da-vinci-robotic-surgery/about-the-systems.

[4] U. Hagn, M. Nickl, S. Jörg, G. Passig, T. Bahls, A. Nothhelfer, F. Hacker, L. Le-Tien, A. Albu-Schäeffer, R. Konietschke, M. Grebenstein, R. Warpup, R. Haslinger, M. Frommberger and G. Hirzinger, "The DLR MIRO: A versatile lightweight robot for surgical applications," in Industrial Robot: An International Journal, vol. 35, pp. 324–336, June 2008.

[5] H. Lv, G. Yang, H. Zhou, X. Huang, H. Yang and Z. Pang, "Teleoperation of Collaborative Robot for Remote Dementia Care in Home Environments," in IEEE Journal of Translational Engineering in Health and Medicine, vol. 8, pp. 1–10, June 2020.

[6] S. Parsa, H. A. Major, A. R. E. Thumwood, M. L. Wilson, M. Hanheide, A. M. Ghalamzan E., "The Impact of Motion Scaling and Haptic Guidance on Operators' Workload and Performance in Teleoperation," in Extended Abstracts of the 2022 CHI Conference on Human Factors in Computing Systems, pp. 1–7, April 2022.

[7] L. B. Rosenberg, "Virtual fixtures: Perceptual tools for telerobotic manipulation," in IEEE Virtual Reality Annual International Symposium, pp. 76–82, September 1993.

[8] R. Moccia, C. Iacono, B. Siciliano and F. Ficuciello, "Vision-Based Dynamic Virtual Fixtures for Tools Collision Avoidance in Robotic Surgery," in IEEE Robotics and Automation Letters, vol. 5(2), pp. 1650–1655, January 2020.

[9] M. Selvaggio, A. M. Ghalamzan E., R. Moccia, F. Ficuciello and B. Siciliano, "Haptic-guided shared control for needle grasping optimization in minimally invasive robotic surgery," in 2019 IEEE/RSJ International Conference on Intelligent Robots and Systems (IROS), pp. 3617–3623, November 2019.

[10] Y. Cai, P. Choi, C.-W. V. Hui, R. H. Taylor and K. W. S. Au, "A Task Space Virtual Fixture Architecture for Teleoperated Surgical System With Slave Joint Limit Constraints," in IEEE/ASME Transactions on Mechatronics, vol. 27(1), pp. 69–80, February 2022.

[11] W. Chen, J. Zhou, S. S. Cheng, Y. Lu, F. Zhong, Y. Gao, Y. Wang, L. Xue, M. C. F. Tong and Y.-H. Liu, "Tele-Operated Oropharyngeal Swab (TOOS) Robot Enabled by TSS Soft Hand for Safe and Effective Sampling," in IEEE Transactions on Medical Robotics and Bionics, vol. 3(4), pp. 1040–1053, November 2021.

[12] H. Zhang, L. Zhu, J. Shen and A. Song, "Implicit Neural Field Guidance for Teleoperated Robot-assisted Surgery," in 2023 IEEE International Conference on Robotics and Automation (ICRA), pp. 6866–6872, July 2023.

[13] Y. Fan, J. Luo, L. Zuo and N. Wang, "A Regulable Linear Guidance Flexible Virtual Fixture Based on EMG in Teleoperation System," in 2021 26th International Conference on Automation and Computing (ICAC), pp. 1–6, September 2021.

[14] F. Ferraguti, C. Secchi and C. Fantuzzi, "A tank-based approach to impedance control with variable stiffness," in 2013 IEEE International Conference on Robotics and Automation (ICRA), pp. 4948–4953, 2013.

[15] S. A. Schwarz and U. Thomas, "Variable Impedance Control for Safety and Usability in Telemanipulation," in 2022 IEEE/RSJ International Conference on Intelligent Robots and Systems (IROS), October 2022.

[16] Y. Ding and U. Thomas, "Improving Safety and Accuracy of Impedance Controlled Robot Manipulators with Proximity Perception and Proactive Impact Reactions," in 2021 IEEE International Conference on Robotics and Automation (ICRA), pp. 3816–3821, Mai 2021.

[17] C. Ott, "Cartesian Impedance Control of Redundant and Flexible-Joint Robots," Springer Tracts in Advanced Robotics (STAR), vol. 49, Berlin, Germany: Springer-Verlag, 2008.

[18] S. A. Schwarz, C. Gaebert and U. Thomas, "6D Dynamic Tool Compensation using Deep Neural Networks to improve Bilateral Telemanipulation," in 2nd Workshop Toward Robot Avatars - ICRA, Mai 2023.

[19] GOOGLE LLC 2020, "MediaPipe Face Mesh," accessed on 26.02.2024 at https://google.github.io/mediapipe/solutions/face_mesh.html.

[20] G. Bradski, "The OpenCV Library," in Dr. Dobb's Journal of Software Tools, 2000.

[21] K. H. Strobl and W. Sepp and S. Fuchs and C. Paredes and M. Smisek and K. Arbter, "DLR CalDe and DLR CalLab," from Institute of Robotics and Mechatronics, German Aerospace Center (DLR) at Oberpfaffenhofen, Germany. Accesson on 26.02.2024 at http://www.robotic.dlr.de/callab/.

[22] A. van der Schaft, "L2-Gain and Passivity Techniques in Nonlinear Control," Cham Springer International Publishing, 2017.